Combined Molecular Graph Neural Network and Structural Docking Selects Potent Programmable Cell Death Protein 1/Programmable Death-Ligand 1 (PD-1/PD-L1) Small Molecule Inhibitors

Prageeth R. Wijewardhane,[#,1] Krupal P. Jethava,[#,1] Jonathan A. Fine,[#,1] Gaurav Chopra*[,1,2]

[1]Department of Chemistry, Purdue University, 560 Oval Drive, West Lafayette, IN, USA

[2]Purdue Institute for Drug Discovery, Integrative Data Science Institute, Purdue Center for Cancer Research, Purdue Institute for Inflammation, Immunology and Infectious Disease, Purdue Institute for Integrative Neuroscience, West Lafayette, IN, USA

# These authors share an equal contribution to this work

*Corresponding author

ABSTRACT

The Programmable Cell Death Protein 1/Programmable Death-Ligand 1 (PD-1/PD-L1) interaction is an immune checkpoint utilized by cancer cells to enhance immune suppression. There exists a huge need to develop small molecules drugs that are fast acting, cheap, and readily bioavailable compared to antibodies. Unfortunately, synthesizing and validating large libraries of small-molecule to inhibit PD-1/PD-L1 interaction in a blind manner is a both time-consuming and expensive. To improve this drug discovery pipeline, we have developed a machine learning methodology trained on patent data to identify, synthesize and validate PD-1/PD-L1 small molecule inhibitors. Our model incorporates two features: docking scores to represent the energy of binding (E) as a global feature and sub-graph features through a graph neural network (GNN) to represent local features. This Energy-Graph Neural Network (EGNN) model outperforms traditional machine learning methods as well as a simple GNN with an average F1 score of 0.997 (± 0.004) suggesting that the topology of the small molecule, the structural interaction in the binding pocket, and chemical diversity of the training data are all important considerations for enhancing model performance. A Bootstrapped EGNN model was used to select compounds for synthesis and experimental validation with predicted high and low potency to inhibit PD-1/PD-L1 interaction. The new potent inhibitor, (4-((3-(2,3-dihydrobenzo[*b*][1,4]dioxin-6-yl)-2-methylbenzyl)oxy)-2,6-dimethoxybenzyl)-D-serine, is a hybrid of two known bioactive scaffolds, and has an IC_{50} values of 339.9 nM that is comparatively better than the known bioactive compound. We conclude that our EGNN model can identify active molecules designed by scaffold hopping, a well-known medicinal chemistry technique and will be useful to identify new potent small molecule inhibitors for specific targets.

INTRODUCTION

Programmed cell death protein 1 (PD-1) is an immune checkpoint receptor implicated for the creation of new cancer therapeutics.[1] The prolonged interaction between the T-cell receptor and the major histocompatibility complex (MHC) leads to upregulation of PD-1 on the activated T-cell surface.[2] Activated T cells produce cytokines, such as Interferon-γ, which in turn cause tumor cells to express programmed death ligand 1 (PD-L1) on the their cell surface.[2] Tumors escape the action of immune system by utilizing the interaction between PD-1 and ligand PD-L1 resulting in lower effector T-cell function and survival, as such resulting in a suppressive immune response in the tumor microenvironment.[2] The inhibition of the PD-1/PD-L1 interaction can enhance anti-tumor immunity and a large amount of work has been done to develop monoclonal antibodies as inhibitors of PD-1/PD-L1 interaction inhibitors.[3,4] For example, Pembrolizumab and cemiplimab, and nivolumab are three FDA approved anti-PD-1 antibodies.[4] The discovery of small-molecule inhibitors would be an advantageous over antibodies, such as being fast-acting, simple for *in vivo* administration, ability to penetrate through cell membranes and interact with the cytoplasmic domains of cell surface receptors.[5] Since a few years, there has been significant development in designing PD-1/PD-L1 inhibitors.[6,7] Specifically, Bristol-Myers Squibb (BMS) discovered a set of potent PD-1/PD-L1 small molecule inhibitors based on the peptidomimetic molecules and non-peptidic small molecules.[6,7] In particular, BMS revealed a 2-methyl-3-biphenyl-methanol scaffold containing chemical libraries. Later, Holak *et al*. studied the interaction of BMS molecules with PD-L1 suggesting that BMS molecules induce PD-L1 dimerization and also reported crystal structures of compounds with dimeric PD-L1.[8,9] Based on these findings, we envisioned to develop a machine learning (ML) framework for selecting and testing new PD-1/PD-L1 inhibitors.

Traditionally, the development of small-molecule inhibitors requires high throughput screening of a large library of diverse drug-like compounds[10] or a medicinal chemist iterating over a scaffold with weak receptor activity to enhance potency.[11] This entire process is – (i) time consuming; (ii) needs expensive instrumentation and robotics; (iii) based on trial-and-error; and (iv) highly inefficient to identify several new scaffolds rapidly.[12] In addition, virtual screening using docking methods have been developed to improve this process but with limited success.[13] Further, ML architectures such as Support Vector Machine (SVM)[14–16], Random Forest (RF)[17–19], Graph Convolution Network[20], and Graph Neural Networks (GNN)[21,22] have been used for drug design and predicting drug-target interactions[23,24]. Recently, new architectures utilizing a combination of graph features in the binding site of a protein have shown great promise for calculating binding affinities and determining whether a compound will bind to a target.[20,22]

Several new neural network-based architectures have also been proposed that show promise to identify potent scaffolds, but many have not been tested experimentally,[15,16,25–28] and developments in the ability to mine and characterize protein crystallography data hopes to drive the creation of these models.[29] Recently, it has been shown that molecular sub-graph features incorporated through a GNN and protein features encoded by their sequence can be combined to predict if a compound can target a given protein.[24] Inspired by this work and based on our interest in developing methods for drug design and immunology[29–36], we have developed a new machine learning model to predict if a compound can inhibit the PD-1/PD-L1 interaction. Our method replaces the protein sequence features with docking scores representing the free energy of binding and due to this global energetic interaction of the small molecule in the binding pocket, we have termed this model as an “Energy Graph Neural Network” (EGNN). The three-dimensional atomic interaction energetic scores are calculated using CANDOCK[31] (**Figure 1B**) and are combined with local molecular graph features (**Figure 1A**) using an end-to-end training methodology (**Figure 1C-D**). In this work, we use this EGNN model to select designs for synthesis, and experimentally test a curated list of compounds from these predictions to prospectively identify potent PD-L1 small molecule inhibitors using the Homogenous Time-Resolved

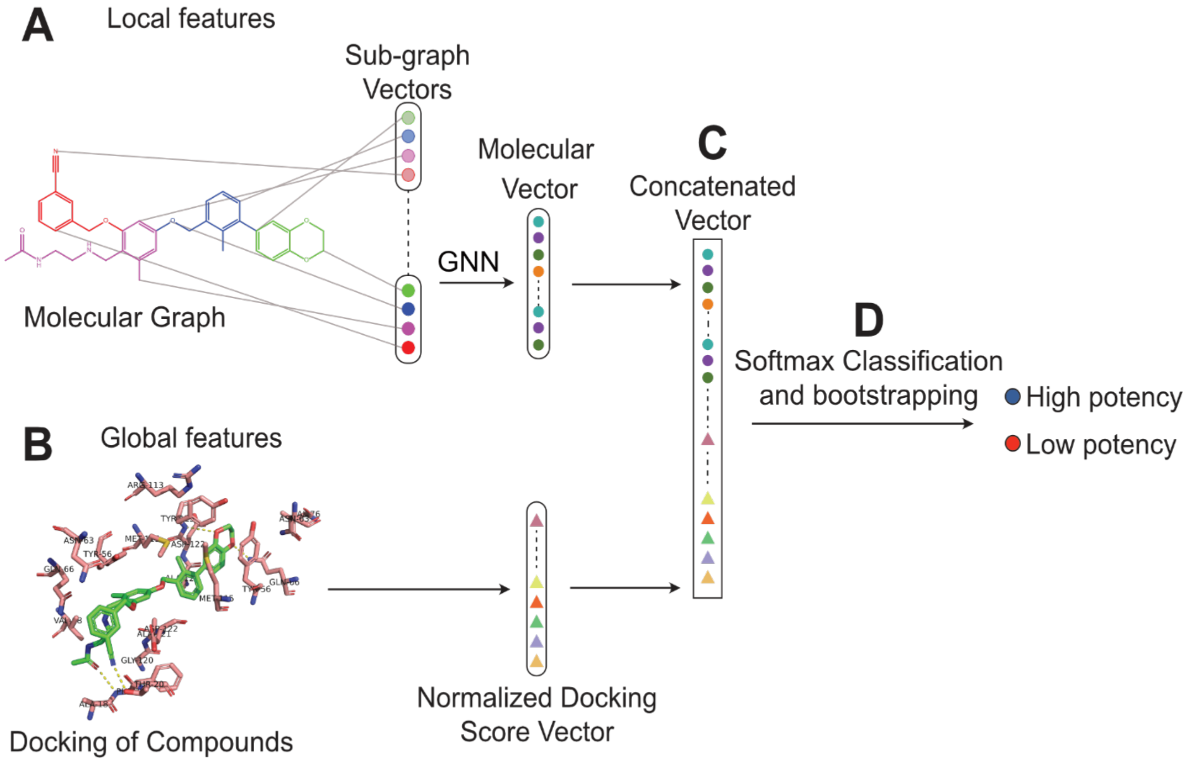

Figure 1. The EGNN model takes advantage of a combination of local (A) and global (B) features. The local features are calculated from the molecular graph of a molecule using a GNN to assign weights to various sub-graphs of the molecule. The global features are a collection of docking scores used to represent the interactions between the compound and protein. These two features are combined to create a concatenated vector (C) which is passed through a SoftMax layer and bootstrapped to classify a molecule as having ‘low’ or ‘high’ potency against PD-1/PD-L1 interaction.

Fluorescence (HTRF) assay. We also tested negative predictions suggesting the utility of the model to be used for selecting potent leads as PD-1/PD-L1 inhibitors.

RESULTS

Patent Data for Training the EGNN Model

We used PD-1/PD-L1 small molecule inhibition data for 464 compounds from three patents to train our models: WO 2015/160641 A2 by BMS (376 compounds)[6], and WO 2018/119263 A1[37] and US 2018/0273519 A1[38] by Incyte Corporation (88 compounds). We did not consider the

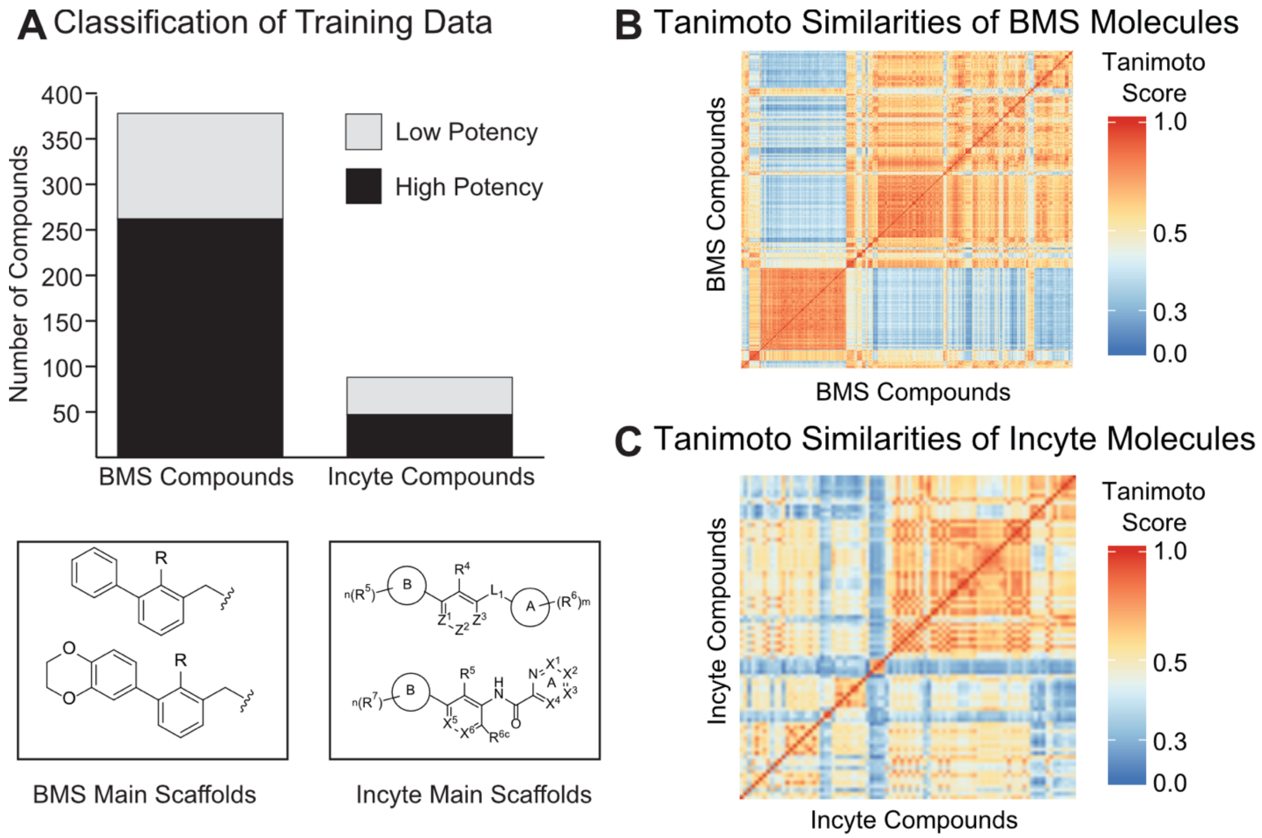

Figure 2. (A) Upper: Classification of Training Data in BMS and Incyte Patents. Bottom: Left: Main PD-L1 inhibitor scaffolds of BMS patents. R group can be CN, Cl, Br, or CH_3. Right: Main PD-L1 inhibitor scaffolds of Incyte patents. Here A and B denote sub-scaffolds. (B) & (C) Heatmaps of pairwise Tanimoto similarity scores of BMS and Incyte compounds respectively.

other BMS patent WO 2015/034820 A1[7] as it contains similar scaffold present in the WO 2015/160641 A2 patent[6] with minor changes. A homogeneous time-resolved fluorescence (HTRF) binding assay was used to show activity against PD-1/PD-L1 interaction in the patents. However, the patents did not list individual IC_{50} values for all compounds but provided a range of inhibition with the different molecules. Therefore, we trained a binary classifier with cutoffs for both datasets to treat a molecule as "High potency" or "Low potency" (**Figure 1**). If the reported IC_{50} of a molecule is less than or equal to 100 nM in the patent it was considered as a "High potency" molecule, otherwise it was considered as a "Low potency" molecule. This threshold yields 307 high potency molecules and 157 low potency molecules for use in training and validating machine learning models; approximately 2:1 split between high potency and low potency molecules. It should be noted that the actual value of IC_{50} should not be considered here as our experiments with multiple replicates were not able to obtain exactly reported results for some molecules in the patents (see IC_{50} value of compound **4a** in **Table 2**, BMS-1 with 6-100 nM annotated in the WO 2015/034820 A1 patent[7]). Therefore, we consider positive prediction (high potency) based on our experimental IC_{50} value as compared to the upper limit of a BMS control molecule (compound **4a**/BMS-1) in WO 2015/034820 A1 patent[7] that is not included in the training set. The annotated training dataset of 464 small molecules is shown in Supporting Information File (**TrainingData.xlsx**).

We selected the BMS and Incyte patents to include chemical diversity of the molecules in the training data set. **Figure 2A** shows the distribution of low and high potency molecules and general scaffolds in the BMS and Incyte patents. The BMS patent has 260 high potency compounds and 116 low potency compounds while the Incyte patents has 47 high potency compounds and 41 low potency compounds respectively. The BMS patent scaffolds contains 246 derivatives of (2-methyl-3-biphenylyl)methanol and 130 derivatives of [3-(2,3-dihydro-1,4-benzodioxin-6-yl)-2-methylphenyl]methanol shown in **Figure 2A (bottom - left)** with R groups as CN, Cl, Br, and CH_3. On the other hand, Incyte patent scaffolds have distinct sub-scaffolds, denoted as A and B in **Figure 2A (bottom – right)**. For Incyte scaffolds, X denotes for either N or C—R groups (R: Alkyl groups). These scaffolds suggest that the chemical diversity of Incyte compounds is higher than that of the BMS patent because the general structures of the compounds in Incyte patents have more structural diversity for sub-scaffolds and atoms. We validated this observation using pairwise Tanimoto similarity scores of BMS and Incyte compounds as shown as heatmaps in **Figure 2B** and **2C**, respectively. Morgan fingerprints with radius of 2 and default bit length were used to calculate pairwise Tanimoto similarities. High red color areas in the BMS heatmap indicates that the molecular pairs are structurally similar to each other. Low red areas in the Incyte heatmap suggests it has more chemical diversity in molecular structures. Furthermore, the average pairwise Tanimoto[39] similarity score of all BMS compounds was found to be 0.5213 and 0.3799 for all Incyte compounds, confirming higher chemical diversity in Incyte compounds as compared to BMS compounds.

PD-L1 homodimer and PD-1/PD-L1 Crystal Structures Reveals a Binding Site for Docking

It has been shown previously that BMS compounds inhibit the PD-1/PD-L1 interaction by inducing dimerization of PD-L1.[8,9] Therefore, a PD-L1 homodimer crystal structure (PDB ID: 5N2F) was selected for docking all the compounds in this manuscript. A PD-1/PD-L1 crystal structure (PDB ID: 4ZQK) was also used to check whether the binding site location of PD-L1 in the homodimer crystal structure (5N2F) overlapped and aligned with each other using the PyMol software package[40](**Figure 3A**). In **Figure 3B,** the selected binding site of the PD-L1 homodimer on the overlapped and aligned crystal structures is shown to indicate that the formation of the homodimer of PD-L1 with small molecules blocks the PD-1/PD-L1 interaction. A known inhibitor of the PD-1/PD-L1 interaction (ligand ID: 8HW)[8] in the selected binding site (**Figure 3C**) suggests that the selected binding site corresponding to PD-L1 homodimers is relevant to develop PD-1/PD-L1 inhibitors. Therefore, the docking interactions of the PD-L1 homodimer will be relevant towards identifying PD-1/PD-L1 inhibitors.

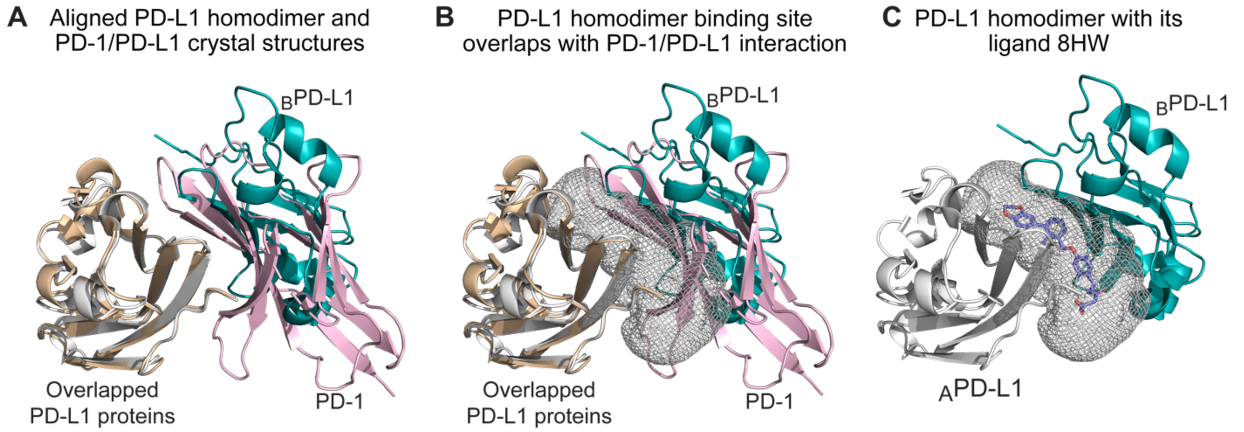

Figure 3. The light pink chain represents the PD-1 protein and the pale cyan chain represents the PD-L1 protein in the PD-1/PD-L1 complex crystal structure (PDB ID: 4ZQK). The wheat color chain represents the PD-L1 chain A and the blue white color represents the PD-L1 chain B in the PD-L1 homodimer crystal structure (PDB ID: 5N2F) (A) Overlapped and aligned PD-1/PD-L1 (4ZQK) and PD-L1 dimer (5N2F) crystal structures. (B) Overlapped and aligned two crystal structures with the determined binding site (grey color mesh) of the PD-L1 dimer (5N2F). (C) The PD-L1 dimer (5N2F) crystal structure with the small molecule (ligand ID: 8HW) at its binding site (grey color mesh).

CANDOCK[31] was used to generate docking conformations of small molecules with PD-L1 homodimer (see Experimental Section on **Generation of Energy Features with Docking and Energy Vector (E) in EGNN** for details). Before developing a machine learning method, we also assessed the ability of only using the docking scores for compounds in the training set for each

96 potential energy scoring function^{31} in CANDOCK to classify the active vs inactive molecules. Two methods were used to select the best scoring function to differentiate between the high and low potency classes. First, Area Under the Receiver Operator Characteristic Curve (AUROC) values were used (**Table S1**). The scoring function, normalized frequency cumulative reduced 15 (FCR15) acquired the highest AUROC value of 0.7855. Second, the best scoring function was selected by comparing the largest difference between the mean docking scores for the high potency and low potency classes (**Table S2**). It suggested that the normalized frequency-mean-complete-15 (FMC15)^{31} scoring function has the highest difference to separate high and low potency classes. Additionally, the AUROC of this function is 0.7729 and is close to that of FCR15. This result is consistent with our previously published assessment of CANDOCK scoring functions to assess biological activity^{31}. However, both FCR15 and FMC15 scores were not able to clearly separate all the high and low potent classified molecules in the training data (see Violin plots in **Figure S1**). Using only one scoring function is not sufficient to capture the different states of PD-1/PD-L1 inhibition with small molecules. Therefore, we developed an EGNN model with 96 different potential function to represent the global features (see Experimental Section on **Generation of Energy Features with Docking and Energy Vector (E) in EGNN** for details).

EGNN Model with Hyperparameter Optimization Outperforms GNN and Other Baseline Models

A detailed description of the EGNN model including a combination of molecular GNN combined with docking is given in the **Experimental Section**. **Figure 1** shows that the EGNN model is a combination of local features of the small molecule represented as a GNN (see **Graph Neural Network for Molecular Graphs in EGNN**) along with global features of protein-ligand interaction represented as docking scores (see section **Generation of Energy Features with Docking and**

Energy Vector (E) in EGNN). The EGNN was trained with 464 small molecules with high and low potency for PD-1/PD-L1 inhibition extracted from patent literature (see **Patent Data for Training the EGNN Model**). We calculated variation in the average F1 score (over five cross-validated folds) compared to number of epochs for different hyperparameters (**Figure S2**). Optimal hyperparameters were selected for EGNN include: dimension of the hidden molecular vector (dim) = 7, sub-graph radius = 2, and number of hidden layers = 1 (see Experimental Section on **EGNN Training and Hyperparameter Optimization**).

The EGNN and GNN models were trained with different training sets to examine the effect of chemical diversity on model performance for classification of active and inactive molecules. Two datasets (BMS and Incyte) were used separately and in combination to train the EGNN model and determine the best dataset to predict PD-1/PD-L1 inhibitors. Here, F1 score and Area Under the Receiver Operator Characteristic Curves (AUROC) were measured to compare three models trained with BMS data only, Incyte data only and BMS-Incyte combine data. AUROC was measured for the model trained only on BMS data while predicting for Incyte data, and vice versa.

Figure 4A shows average F1 scores (over five-fold cross-validation) for both models trained with BMS compounds, Incyte compounds, and the union of these sets. The average F1 scores of the EGNN and GNN models trained with Incyte data were 0.956 (±0.051) and 0.678 (±0.157), respectively (**Figure 4A**). This result suggests that the EGNN trained model with Incyte data that contains diverse chemical scaffolds (**Figure 2C**) performs much better than the GNN trained with the same data set. However, when the same test was done with only BMS compounds with lower chemical diversity than Incyte, the average F1 score is comparable for both models with 0.992 (± 0.007) for the EGNN model and 0.948 (± 0.022) for the GNN model.

This suggests that the GNN model performs well with smaller chemical diversity in the training data as compared to larger chemical diversity in training data. However, the EGNN model performs well with both datasets, indicating that it is a superior model to the GNN.

When both BMS and Incyte datasets were combined, the average F1 score of the EGNN model was 0.997 (± 0.004) and 0.891 (± 0.030) for the GNN model. Although the average F1 score of the EGNN increased slightly by combining both datasets, the average F1 score of the GNN model decreased compared to GNN trained only with BMS compounds (previously 0.948± 0.022).

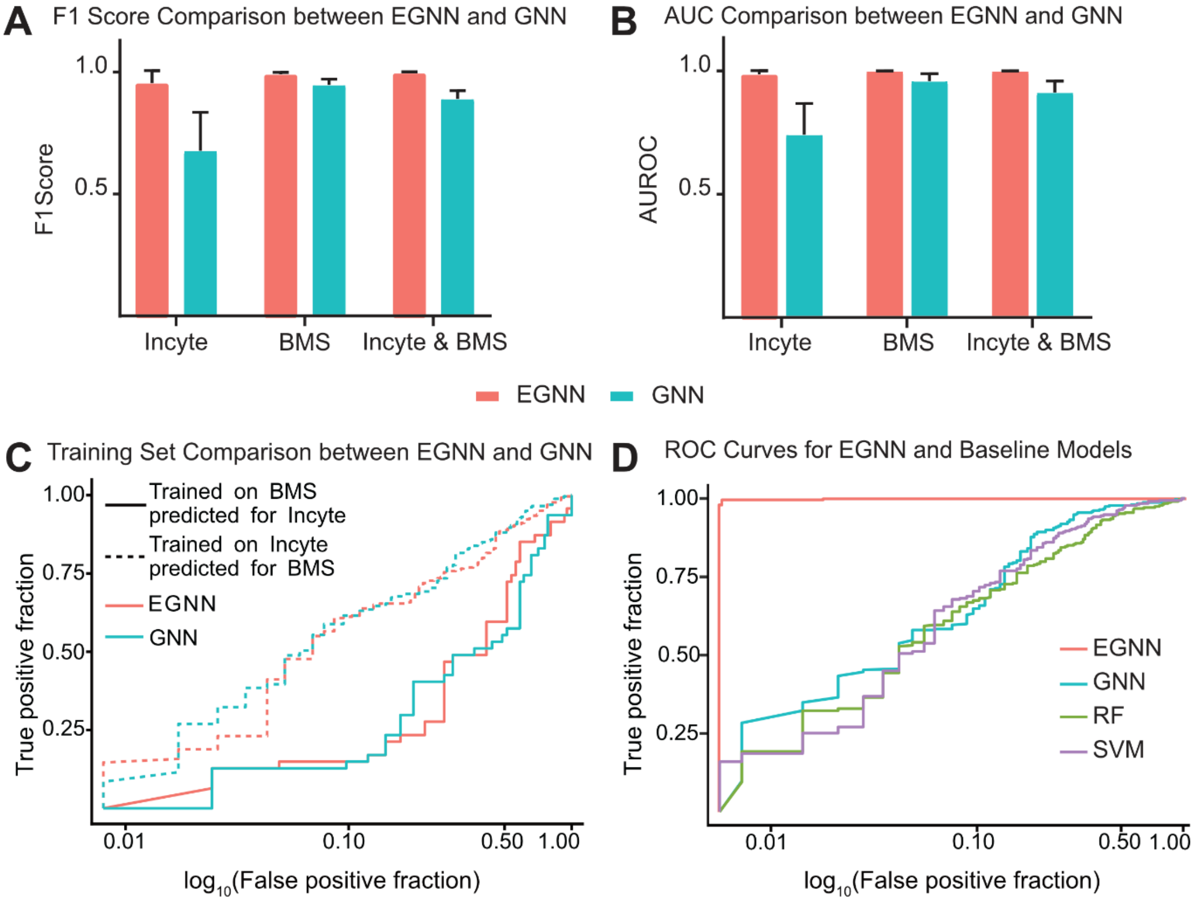

Figure 4. (A) F1 scores for EGNN and GNN with different training and validation/test sets. (B) Area under the curve values for EGNN and GNN models with different training and validation/test sets. (C) ROC curves for different EGNN and GNN models trained on BMS or Incyte data and predict for the other dataset. (D) ROC curves for EGNN, GNN, RF and SVM models trained with combined BMS and Incyte data.

A similar trend is observed for the AUROCs for the three different training set comparisons (**Figure 4B**). These results suggest that the EGNN model outperforms the GNN model for chemically diverse training and validation sets. We believe this to be due to the addition of 'global' energy features captured by the docking scores of PD-L1 homodimers as training data in EGNN compared to only the 'local' structural features of small molecules in the training data for the GNN model.

We also investigated the ability of the EGNN and GNN models trained on one compound set to predict high and low potency inhibitors of PD-1/PD-L1 in the other compound set. These results are represented as ROC curves in **Figure 4C.** When the EGNN and GNN models are trained on BMS compounds and used to predict Incyte compounds, a near random prediction curve is observed for both models with AUROC of 0.6038 for the EGNN and 0.5854 for the GNN. However, the ROC curves for both models improved when they were trained with Incyte data and used to predict the BMS compounds (AUROC of EGNN = 0.8139, GNN = 0.8287). These results suggest that even though there is marked improvement in AUROC values for the EGNN model versus the GNN model, there is no improvement seen in the F1 scores for both EGNN and GNN models (see **Table S3** for details). This highlights the importance of chemical diversity in training data, in that, it is not enough to use only BMS or only Incyte data alone to train the final model to make predictions for unknown molecules. Therefore, we selected the combined BMS-Incyte dataset to train the EGNN model which improved both models (**Table S3**).

Finally, we compared the cross-validated EGNN model with GNN, SVM, and RF baseline models trained with BMS-Incyte combined training data. Both SVM and RF models are trained on 96 docking scores obtained by CANDOCK ('global' energy features). Precision, recall, AUROC and

F1 score values are tabulated in the **Table 1** for all four models. The SVM model was trained using the caret package with the "svmRadial" method[41] and the RF was trained using the 'randomForest' library in R with 500 trees using caret[41] package for statistics precision, recall and F1 score. AUROC values were calculated using pROC[42] library. The EGNN model outperforms all other models with values of 0.996, 0.997, 0.999, and 0.997 for precision, recall, AUROC and average F1 score, respectively (**Table 1**). Comparing ROC curves of these four models (**Figure 4D**) also confirmed that the EGNN model outperforms all three other models. Hence, neither only topology of the small molecules ('local' features), nor only the docking scores ('global' features) of compound-protein interactions are enough to classify small molecules as PD-1/PD-L1 high and low potency inhibitors. Taken together, the combined local and global features in EGNN gives the best performance on BMS-Incyte combined training and validation set.

Table 1. Precision, Recall, AUROC and F1 Score of the EGNN for PD-1/PD-L1 inhibitor predictions compared to other baseline models, such as, Random Forest, SVM, and GNN models. All models were trained on the combined BMS and Incyte dataset.

Measure	**Model**			
	Random Forest	**SVM**	**GNN**	**EGNN**
Precision	0.720	0.778	0.866	0.996
Recall	0.688	0.758	0.921	0.997
AUROC	0.881	0.900	0.910	0.999
Average F1 Score	0.704	0.768	0.891	0.997

Synthetic Selection and Validation of EGNN Predictions for PD-1/PD-L1 Inhibition

The EGNN model trained with optimum hyperparameters and the combined dataset was used to get predictions for an in-house database of small molecular designs. We developed a bootstrapped EGNN model to predict compounds with high and low potency for PD-1/PD-L1 inhibition using 1000 EGNN models (see section **Bootstrapping the EGNN model**). Bootstrapping is an essential statistical technique that can be used to select confident molecules for synthesis and experimental validation based on agreements among multiple models. The bootstrapped GNN model identified high and low potency small molecules as PD-1/PD-L1 inhibitors that were synthesized and then experimentally verified with HTRF binding assay (see **Table 2** for summary). Specifically, we selected 3 molecules predicted to be active or inactive for PD-1/PD-L1 inhibition for testing based on bootstrapped EGNN SoftMax average scores and standard deviation (see EGNN SoftMax scores in **Table 2**).

Out of EGNN bootstrapped predictions, we have selected 1 molecule as active (compound **4b**) and 2 molecules with different scaffolds as inactive (compound **4c** and **4d**) for further testing. Specifically, all 1000 EGNN models resulted in an average SoftMax score of 0.9997 (±0.0029) for compound **4b** suggesting active PD-1/PD-L1 inhibitor prediction. In contrast, only 849 EGNN models resulted in an average SoftMax value of 0.8362 (±0.3025) for compound **4c** and 617 EGNN models resulted in an average SoftMax value of 0.6107 (±0.4351) for compound **4d** suggesting inactive predictions. We also synthesized a BMS scaffold (compound **4a** a known PD-1/PD-L1 inhibitor) for use as a positive control for our HTRF experiments. The compound structures are shown in **Scheme 1** and **2** (see **Experimental Section** for procedures and characterization). The predicted active molecule (compound **4b**) is (4-((3-(2,3-dihydrobenzo[*b*][1,4]dioxin-6-yl)-2-

methylbenzyl)oxy)-2,6-dimethoxybenzyl)-D-serine, a hybrid of two BMS molecules, **4a** (BMS-1) and BMS-1002 containing (2-methyl-3-biphenylyl)methanol and [3-(2,3-dihydro-1,4-benzodioxin-6-yl)-2-methylphenyl]methanol, respectively (**Figure 5A**). This suggests the ability of EGNN model to do scaffold hopping since analogs of BMS-1 and BMS-1002 scaffolds exist in the training data[6].

Scheme 1. Representative Synthesis Scheme[a]

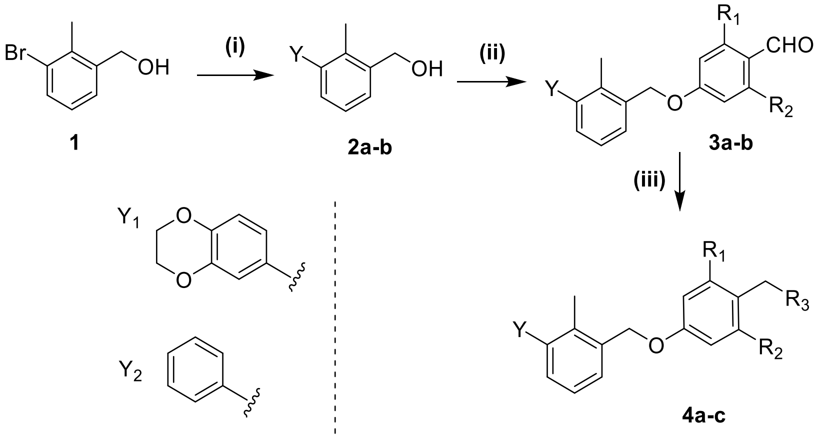

Compound	Y	R_1	R_2	R_3
4a (KPGC01S94)	Y_2	OMe	OMe	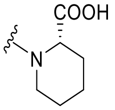
4b (KPGC01S32)	Y_1	OMe	OMe	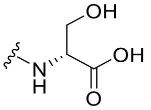
4c (KPGC01S138)	Y_2	OMe	OMe	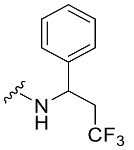

[a] Reaction conditions: (i) BH_3•THF complex (1.0 M in THF), Anhydrous THF, 0 °C to rt, 2 days; (ii) PPh_3, DIAD, 0 °C to rt, 20 h, anhydrous THF; (iii) amine component, $NaBH_3CN$, cat. AcOH, DMF, 80 °C or room temperature, 1h or 3 h or overnight.

Scheme 2. Synthesis of **4d** (GCL2)

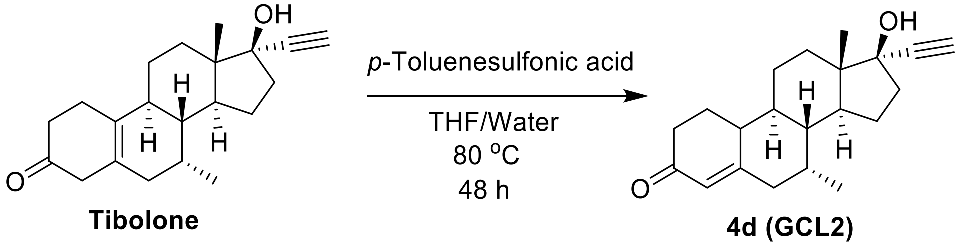

The top docked pose in PD-L1 homodimer (PDB ID: 5N2F) for compound **4b** interacts in a similar manner as shown previously for the co-crystal structures[8] (**Figure 5B**). Specifically, for compound **4b**, the 2,3-Dihydro-1,4-benzodioxine group facilitated the movement of the amino acid residue Tyr56 in chain A of the PD-L1 homodimer ($_A$Tyr56). It is known that this $_A$Tyr56 does not close the hydrophobic pocket from one end if this 2,3-Dihydro-1,4-benzodioxine group is present[8] creating a hydrophobic tunnel (**Figure 5B** inset) rather than a hydrophobic cleft in the docked conformation. Additionally, the aromatic ring of compound **4b** (2,3-Dihydro-1,4-benzodioxine) was stabilized by π-π stacking interactions with the amino acid residue $_A$Tyr56 (**Figure 5C**). The central methylbenzyl ring (magenta color in **4b** in **Figure 5A**) in the structure is rotated by approximately 30° to 2,3-Dihydro-1,4-benzodioxine ring and the methyl group of the methylbenzyl ring point towards chain B of the PD-L1 homodimer. This orientation results in hydrophobic interactions with Met115 of both chain A and B of the homodimer and with $_B$Ala121. The D-serine end of the **4b** compound forms hydrogen bonds with $_A$Thr20 and $_A$Ala121 along with a plausible hydrogen bond formation between backbone NH of $_A$Tyr123 and the oxygen in one of the two methoxy groups of the **4b** molecule (**Figure 5C**). These results suggest favorable interactions of compound **4b** that could dimerize PD-L1 will result in PD-1/PD-L1 inhibition.

The HTRF assay confirmed that compound **4b** has an IC$_{50}$ of 339.9 nM (see **Experimental Section** for details) to inhibit PD-1/PD-L1 interaction (**Figure 5D**). This is comparatively better

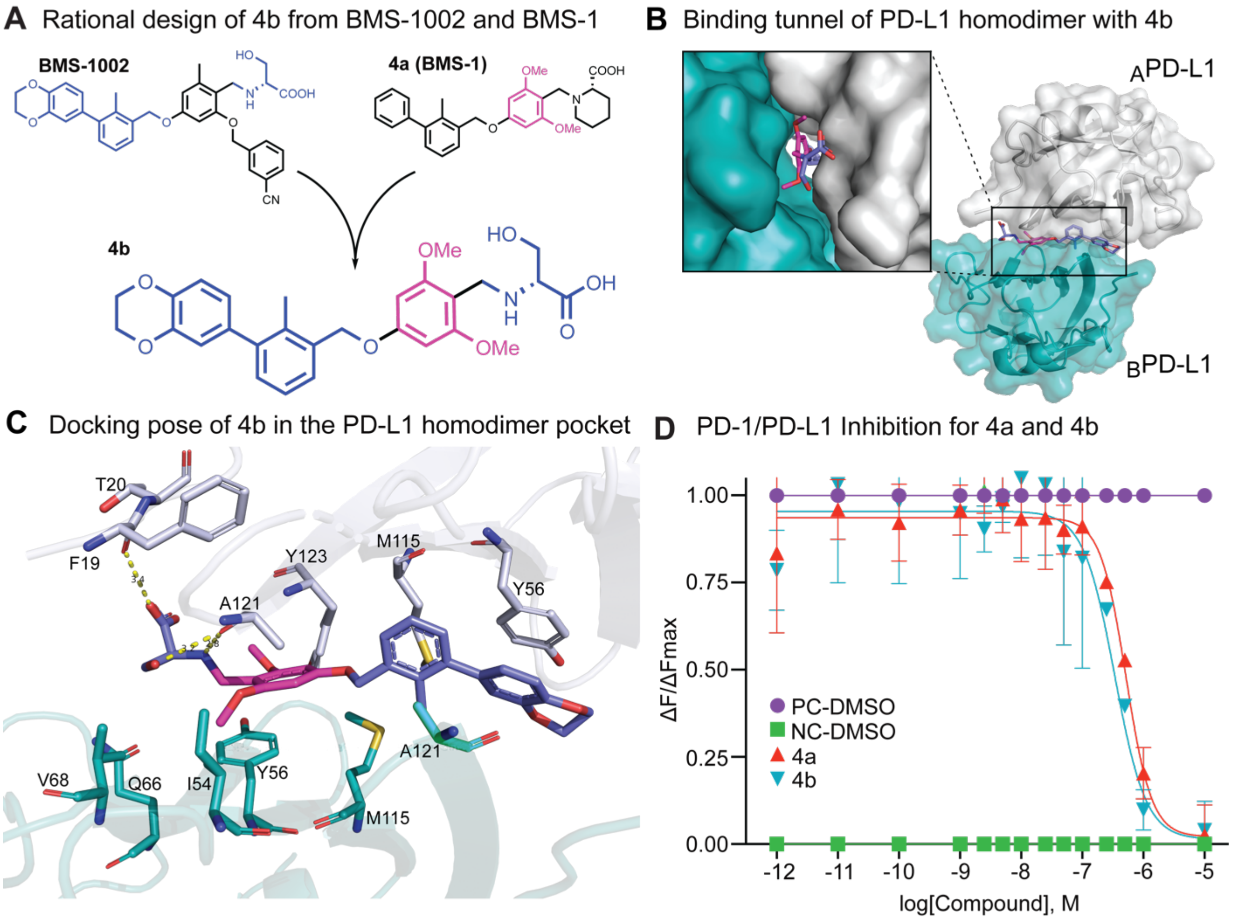

Figure 5. **A.** EGNN predicted a new PD-1/PD-L1 inhibitor, compound **4b**, by scaffold hopping of BMS compounds, **4a** or **BMS-1** and **BMS-1002**. Blue colored parts of the **4b** are added from the **BMS-1002** and pink color part was added from the **4a** (**BMS-1**). **B.** Showing location of top docked pose of the compound **4b** in PD-L1 homodimer crystal structure (PDB ID: 5N2F). Inset showing hydrophobic tunnel for compound **4b**. **C.** Showing chemical interactions of top docked pose interactions of the compound **4b** in PD-L1 homodimer. Blue and pink colored parts are shown as sticks for **4b**. The dotted yellow lines between the compound and the residues ${}_{A}$Thr20 and ${}_{A}$Ala121 represent hydrogen bonding. The orientation of the aromatic ring of tyrosine, ${}_{A}$Tyr56, suggests a plausible π- π interaction with 2,3-dihydro-1,4-benzodioxin blue colored aromatic ring in the compound **4b**. **D.** Comparison of IC$_{50}$ values of **4a** (BMS-1 control compound, red color) and new compound **4b** (blue color). The DMSO controls for positive (PC-DMSO, purple color) and negative controls (NC-DMSO, green color) of the assay are shown for each tested concentration.

than the IC_{50} of 521.5 nM for the BMS compound **4a** that was synthesized and tested in our lab (BMS-1 molecule in the BMS patent WO 2015/034820 A1). It should be noted that the BMS-1 molecule was denoted with the IC_{50} of 6-100 nM with HTRF assay in the BMS patent[7] . However, multiple replicates of our experiments did not result in the IC_{50} value less than 100 nM to inhibit PD-1/PD-L1 interaction (see **Calculation of IC_{50} values** section and Supporting File **HTRF_IC50_Data.xlsx**). As mentioned previously, this result does not affect our machine learning method since we have classified molecules based on high and low potency, compared to developing a model to estimate the specific IC_{50} value. A possible explanation of this difference in experimental results between our work and the patent could be the exact protocol used to perform the HTRF assay and calculation of IC_{50} values. For this reason, we have included a detailed account of HTRF assay protocol, analysis of data for calculation of IC_{50} and supporting data files for use by the scientific community (see **Experimental Section**). In order to test the validity of our bootstrapped EGNN model to correctly identify inactive or low potency predictions, we also tested compounds **4c** and **4d** resulting in no inhibition to PD-1/PD-L1 interaction (**Table 2**). The IC_{50} plots for each compound tested (**Figure S3**) as well as the ^{13}C and ^{1}H NMR spectra are provided as **Supporting Information**. Taken together, these results suggest that bootstrapped EGNN model can be used to select molecules for synthesis and experimental validation of PD-1/PD-L1 inhibition.

Table 2. IC_{50} values for predicted active and inactive compounds with EGNN SoftMax scores

Compound	IC_{50} value	SoftMax score	Prediction
4a (KPGC01S94)	521.5 nM	Control*	Control*
4b(KPGC01S32)	339.9 nM	0.9997 +/- 0.0029	Active

4c (KPGC01S138)	no inhibition	0.8362 +/- 0.3025	Inactive
4d (GCL.2)	no inhibition	0.6107 +/- 0.4351	Inactive

*denotes BMS active compound

DISCUSSION AND CONCLUSION

Cancer immunotherapy marks a major step in treating cancer and the development of PD-1/PD-L1 immune checkpoint inhibitors have been an important area of research for treatment of several tumors. Currently, six therapeutic antibodies targeting both PD-1 (pembrolizumab, nivolumab, and cemiplimab) and PD-L1 (atezolizumab, durvalumab, and avelumab) have been approved by U.S. FDA. Recently, several new small molecules PD-1/PD-L1 inhibitors have been developed[43] along with structure determination of human PD-1/PD-L1 complex and cocrystals of inhibitory ligands[44–46]. Still the field is very active in search for new small molecules to inhibit this important checkpoint and we hope to enhance the speed of this search with the use of new structure-based ML methods that have been benchmarked extensively and tested prospectively.

We have developed a new ML methodology, EGNN, based on combining local features of the small molecule topology and global features of the small molecule interacting within the binding pocket as energetic scores to select, synthesize and experimentally validate potent inhibitors of PD-1/PD-L1 interaction. Specifically, EGNN outperforms traditional ML architectures, such as, RF, SVM that include only global features, as well as the GNN model that uses only local features of small molecular topology. When benchmarked with known PD-1/PD-L1 inhibitors from BMS and Incyte patents data, we concluded that topology of the small molecule, the structural interaction in the binding pocket, and chemical diversity of the training data are all important considerations for enhancing model performance.

We used a bootstrapped EGNN model (based on 1000 EGNN models) for prediction and confident selection of new molecules for chemical synthesis and subsequent testing of inhibition using HTRF PD-1/PD-L1 inhibition assay. We believe that bootstrapping is an important statistical technique to use with ML methods to confidently select molecules for experimental validation in drug design. The predicted active molecule, (4-((3-(2,3-dihydrobenzo[*b*][1,4]dioxin-6-yl)-2-methylbenzyl)oxy)-2,6-dimethoxybenzyl)-D-serine, is a hybrid of two BMS active molecular scaffolds, and has an IC_{50} value of 339.9 nM for inhibiting PD-1/PD-L1 interaction, suggesting the ability of EGNN model to do scaffold hopping to identify new inhibitors. Accurate selection of inactive molecules with different scaffolds suggests practical utility of our bootstrapped model for selection of compounds for synthesis, a hard problem in the field of ML based drug design.

Our EGNN methodology can be further developed with the addition of more chemically diverse publicly data, in-house training and validation dataset, and incorporating reinforcement iterative learning with experiments performed in each step for developing a library of structurally diverse small molecule inhibiting PD-1/PD-L1 interaction to guide structure-activity relationships. Given the general nature of the machine learning model and docking methodology that is readily available for use, this approach can be adapted to identify small molecule immunomodulators by targeting other immune checkpoints, as well as, generally used to include local and global features for target-based drug design.

EXPERIMENTAL SECTION

Homogenous Time-Resolved Fluorescence (HTRF) Assay to Test Inhibition of Predicted Compounds

Inhibition of PD-1/PD-L1 interaction was tested for 3 active and inactive predicted compounds using the PD1/PD-L1 HTRF assay kit from Cisbio US, Inc. The assay protocol was used as mentioned in the kit for each predicted compound (**4b, 4c, GCL.2**) and the BMS control compound (**4a**). Briefly, 2 µL of the compound, 4 µL from a 25 nM Tag1-PD-L1 protein solution and 4 µL from a 250 nM Tag2-PD1 protein were added into a Cisbio's HTRF 96-well low volume white plate. Then, the plate was incubated for 15 minutes at room temperature. Next, 10 µL from pre-mixed anti-tag detection reagents (5 µL from 1X anti-Tag1-Eu^{3+} and 5 µL from 1X anti-Tag2-XL665) were added and the sealed plate was incubated for 2 hours at room temperature. Finally, the plate sealer was removed, and measurements were taken using a HTRF® compatible reader. This protocol used 12 different concentrations of each compound where the maximum and minimum assay concentrations are 10,000 nM and 0.001 nM respectively. Several replicates at different concentration were done for active prediction compound **4b** (36 data points) and positive control compound **4a** (48 data points). The fitted curve for normalized signal denoted by $\Delta F/\Delta Fmax$ (calculated using HTRF ratio 665 nm/620 nm) versus log[concentration] was used to determine the 50% inhibitory concentrations (IC_{50}) of the compounds (see next section on **Calculation of IC_{50} values**).

To calculate $\Delta F/\Delta Fmax$, first the HTRF ratio is calculated as follows;

$$HTRF\ ratio = \frac{Signal\ 665\ nm}{Signal\ 620\ nm} \times 10000$$

A multiplication factor of 10000 factor was used to not deal with decimal values that improves data accuracy during calculation. The ΔR ratio indicating "specific signal" of the compound disrupting the PD-1/PD-L1 interaction was calculated by subtracting background HTRF ratio (negative DMSO control in our work) from each compound (sample) HTRF ratio as follows;

$$\Delta R = HTRF\ ratio\ (sample) - HTRF\ ratio\ (background)$$

Next, data normalization was done to minimize variation in values on different days, different plate reader instruments, or if the assay was done by different individuals. The normalization was done with respect to the background HTRF ratio and was calculated as follows;

$$\Delta F = \frac{HTRF\ ratio\ (sample) - HTRF\ ratio\ (background)}{HTRF\ ratio\ (background)} \times 100\%$$

Finally, the $\Delta F/\Delta Fmax$ ratio was calculated to enable comparison of values between multiple experiments.

$$\Delta F/\Delta Fmax = \frac{\Delta F\ (sample)}{\Delta F\ max}$$

where $\Delta F\ max$ is taken as the ΔF of the positive DMSO control in the assay.

Calculation of IC$_{50}$ values

The IC$_{50}$ value for PD-1/PD-L1 inhibition was determined by analyzing the log of the concentration−response curves to fit a sigmoid curve with four-parameter logistic (4PL) regression using the GraphPad Prism Software version 8.3.0 for Windows, GraphPad Software, La Jolla California USA, www.graphpad.com. The IC$_{50}$ values are provided in **Table 2**. Following equation defines the regression curve.

$$Y = Bottom + \frac{(Top - Bottom)}{\left(1 + 10^{((LogIC50 - X) \times HillSlope)}\right)}$$

where X = Log of concentration, Y = Response $\Delta F/\Delta Fmax$, Top and $Bottom$ = Plateaus in same units as Y, $LogIC50$ = Same log units as X, $HillSlope$ = Slope factor or Hill Slope, Unitless. Using the above equation, $LogIC50$, is calculated to obtain the IC_{50} value for each compound. The **HTRF_IC50_Data.xlsx** data file with all replicates is provided as a Supporting File for use in GraphPad Prism Software to calculate IC_{50} values.

Machine Learning Architecture of the EGNN model

The EGNN model was developed using PyTorch[47]. All scripts for implementing the machine learning model and results are provided on GitHub at https://github.com/chopralab/egnn. The **Figure 1** shows the overview of the EGNN machine learning architecture. We implemented the Graph Neural Networks for the molecular graph by Tsubaki and coworkers.[24]. Briefly, the molecular structures were converted into SMILES strings using ChemAxon MolConverter[48] software. Then RDKit[49] software package and the Weisfeiler-Lehman algorithm was used to extract r-radius subgraphs graphs for molecules (**Figure 1A**). The following sections include details of the EGNN architecture.

Graph Neural Network for Molecular Graphs in EGNN

The following equations and notations with details for molecular GNN have been reproduced here from the original work[24] with minor modifications for clarification. The lowercase bold face letters (e.g. $\mathbf{v} \in \mathbb{R}^d$) indicate vectors, uppercase bold face letters (e.g. $\mathbf{M} \in \mathbb{R}^{m \times n}$) indicate matrices, and Italicized non-bold letters (e.g. $S, G, v, \text{and}\ e$) indicate scalars, sets, graphs, vertices, and edges. The GNN converts a molecular graph into a low dimensional real valued vector $\mathbf{y} \in \mathbb{R}^d$ with two neural network-based functions; transition and output.[21] In a graph G, each vertex (v) is updated with considering the information of its neighboring vertices and edges by the transition function. These vertices have been mapped into a real valued vector $\mathbf{y} \in \mathbb{R}^d$ by the output function. Both functions are differentiable. All the input features and weights of the GNN model are updated using back propagation with the help of the cross-entropy loss function.

A graph can be defined as $G = (V, E)$, here; V and E are sets of vertices and edges respectively. When applied to chemistry, atoms can be defined as vertices and chemical bonds can be defined as edges. First, all the atoms and chemical bonds will be embedded as real valued vectors with d-dimensions based on their different types. Since the diversity of atoms (eg: C, N, O, etc.) and bonds (eg: single bonds, double bonds, triple bonds, etc.) in a small molecule is limited, the number of learning parameters are limited. Therefore, a strategy called r-radius sub-graphs[50] was used to avoid this limitation.

r-radius Sub-graphs

The set of all atoms within a defined r radius an atom i can be represented as $N(i, r)$. When the $r = 0$, $N(i, r) = \{i\}$, which is the set of all atoms in the molecule. The r-radius sub-graph of the ith vertex (v_i) is defined as follows;

$$v_i^{(r)} = (V_i^{(r)}, E_i^{(r)})$$

Here,

$$V_i^{(r)} = \{v_j \mid j \in N(i,r)\}$$

$$E_i^{(r)} = \{e_{mn} \in E \mid (m,n) \in N(i,r) \times N(i,r-1)\}$$

The r-radius sub-graph for the edge between ith and jth atoms (e_{ij}) was defined as follows;

$$e_{ij}^{(r)} = (V_i^{(r-1)} \cup V_j^{(r-1)}, E_i^{(r-1)} \cap E_j^{(r-1)})$$

Randomly initialized embeddings (**Figure 1**) are assigned to each r-radius edge $e_{ij}^{(r)}$ and vertex ($v_i^{(r)}$) based on the type. Backpropagation has been used to train these random embeddings.

Vertex Transition Function

Say $\mathbf{v}_i^{(t)} \in \mathbb{R}^d$ is the embedded vector for the i th vertex of a given molecular graph G at time step t. Then the updated $\mathbf{v}_i^{(t+1)} \in \mathbb{R}^d$ vector can be written as follows;

$$\mathbf{v}_i^{(t+1)} = \sigma\left(\mathbf{v}_i^{(t)} + \sum_{j \in N(i)} \mathbf{h}_{ij}^{(t)} \right)$$

Here, $N(i)$ is denoting the set of neighboring atoms, σ is the sigmoid function which is defined as $\sigma(x) = \frac{1}{1+e^x}$, and $\mathbf{h}_{ij}^{(t)} \in \mathbb{R}^d$ is the hidden vector which defines the neighborhood and can be calculated as follows;

$$\mathbf{h}_{ij}^{(t)} = f\left(\mathbf{W}_{neighbor} \begin{bmatrix} \mathbf{v}_j^{(t)} \\ \mathbf{e}_{ij}^{(t)} \end{bmatrix} + \mathbf{b}_{neighbor} \right)$$

Here, f is the Rectified Linear Units (ReLU), a non-linear activation function such $f(x) = max(0,x)$. $\mathbf{W}_{neighbor} \in \mathbb{R}^{d\times 2d}$ and $\mathbf{b}_{neighbor} \in \mathbb{R}^{d\times 2d}$ are the weight matrix and the bias vector respectively. The vector between the ith and jth atoms (vertices) of the molecular graph after the time step t is defined as $\mathbf{e}_{ij}^{(t)}$.

Edge Transition Function

As mentioned before, edge transition function is used to update each embedded edge vector $\mathbf{e}_{ij}^{(t)}$ during the training process.

$$\mathbf{e}_{ij}^{(t+1)} = \sigma\left(\mathbf{e}_{ij}^{(t)} + \mathbf{g}_{ij}^{(t)}\right)$$

$$\mathbf{g}_{ij}^{(t)} = f\left(\mathbf{W}_{edge}\left(\mathbf{v}_{i}^{(t)} + \mathbf{v}_{j}^{(t)}\right) + \mathbf{b}_{edge}\right)$$

Here, $\mathbf{W}_{edge} \in \mathbb{R}^{d\times d}$, $\mathbf{b}_{edge} \in \mathbb{R}^{d\times 1}$ are the weight matrix and the bias vector respectively. Moreover, $\mathbf{v}_{i}^{(t)}$ and $\mathbf{v}_{j}^{(t)}$ are added, because there is no direction for edges in molecular graphs.

Molecular Vector Output of Molecular GNN

The transition function generates an updated set of atom (vertex) vectors $\left(V = \left\{\mathbf{v}_{1}^{(t)}, \mathbf{v}_{2}^{(t)}, \ldots, \mathbf{v}_{|V|}^{(t)}\right\}\right)$. Then the output function uses this set of atom vectors to obtain an unique molecular vector $\mathbf{y}_{molecule} \in \mathbb{R}^{d}$ (**Figure 1A**), which is defined as follows;

$$\mathbf{y}_{molecule} = \frac{\mathbf{1}}{|V|}\sum_{i=1}^{|V|}\mathbf{v}_{i}^{(t)}$$

Here, the total number of vertices in the full molecular graph is denoted by the $|V|$.**Generation of Energy Features with Docking and Energy Vector (E) in EGNN**

First, all the reported molecules were carefully drawn using MarvinSketch[51] software. Then, all the drawn molecules were cleaned in 3D and converted into a sybyl.mol2 file, which was used for docking with our in-house CANDOCK[31] software package (version 0.6.0) using default parameters with 20% top seed percent (**Figure 1B**). CANDOCK source code is available on GitHub at https://github.com/chopralab/candock/releases/tag/v0.6.0. The docking was done with a PD-L1 homodimer crystal structure (PDB ID: 5N2F). We selected the binding site based on the coordinates of the crystal ligand in the protein structure (ligand ID:8HW). Then, radial-mean-reduced-6 (RMR6)[31] was used as "Selector" parameters for docking to select the top pose[31]. Next, the top pose of each docked compound was selected, and its docking score was recalculated using all the available 96 different potential energy functions in CANDOCK[31] software (**Figure 1B**). All 96 CANDOCK docking energy scores of each molecule were normalized for each potential energy function to use as a vector in the EGNN model;

$$\hat{S}_{i,j} = \left(\frac{S_{i,j} - min(S_j)}{max(S_j) - min(S_j)} \right)$$

Where, $i: 1 \rightarrow n$ and $j: 1 \rightarrow m$. Here, n is the number of potential energy scoring functions and m is the number of molecules in the dataset. $\hat{S}_{i,j}$ is the normalized docking energy value for the energy score with ith potential energy function for the jth docked molecule. Similarly, $S_{i,j}$ is the docking energy score before normalization. Also, $max(S_j)$ and $min(S_j)$ are the maximum and minimum energy values within the jth scoring function for all docked molecules. Thus, the normalized docking score vector for each molecule in the EGNN model is represented using all 96 normalized different potential energy scoring functions as $\mathbf{y}_{energy} \in \mathbb{R}^{96}$ (**Figure 1B**).

Output of EGNN

As represented in **Figure 1C**, the normalized docking energy score vector ($\mathbf{y}_{energy}$) is concatenated with the molecular vector output of the GNN ($\mathbf{y}_{molecule}$). Then, the concatenated long vector $(\mathbf{y}_{molecule} \oplus \mathbf{y}_{energy}) \in \mathbb{R}^{(d+96)}$ was used for the training as follows to obtain an output vector $\mathbf{x}_{output} \in \mathbb{R}^2$;

$$\mathbf{x}_{output} = \mathbf{W}_{output}(\mathbf{y}_{molecule} \oplus \mathbf{y}_{energy}) + \mathbf{b}_{output}$$

Here $\oplus$ denotes concatenation**,** $\mathbf{W}_{output} \in \mathbb{R}^{2\times(d+96)}$ denotes the weight matrix and the $\mathbf{b}_{output} \in \mathbb{R}^2$ denotes the bias vector. Then, a SoftMax classifier (**Figure 1D**) is added on to the top of the $\mathbf{x}_{output} = [y_0, y_1]$ vector to get the active or inactive probabilities.

$$p_t = \frac{e^{(y_t)}}{\sum_i e^{(y_i)}}$$

Here, $t \in \{0,1\}$; 0 indicates less potent and 1 indicates highly potent, and the p_t is the probability of the given y_t.

Bootstrapping the EGNN model

The model uses a random number to initialize edge and vertex vectors. Therefore, bootstrapping was used with the final model to get predictions. One thousand different models with distinct random seeds were trained and predictions were obtained for an in-house molecular designs test set. Averaged SoftMax scores were used as the final prediction results of the bootstrapped model. Finally, molecules in the test set were classified as high Potency or low potency based on the averaged SoftMax score. If it is greater or equal to 0.5, it was considered as high Potency, else low potency (**Figure 1**). Thus, the EGNN model will be trained with back propagation with given SMILES strings, the vectors of all 96 scores generated by CANDOCK[31] and their high potency or low potency status with the PD-L1 protein. The trained model can be used to predict the probability of a given molecule to be a high or low potent molecule towards the PD-L1 protein.

EGNN Training and Hyperparameter Optimization

The model takes a SMILES string and a docking energy score string for a given molecule as inputs. Hyperparameters of the model were optimized before using it for predictions. Dimension of the GNN hidden vector (dim), number of hidden layers of the GNN, and sub-graph radius was optimized by considering the five-fold cross validated F1 score. Six values were used for the dimension of the GNN hidden molecular vector output (i.e. dim = 5, 6, 7, 8, 10 and 20). Numbers 1, 2, and 3 were used to check for the optimum number of hidden layers in the GNN. Finally, the optimum sub-graph radius for the model was selected out of radius = 2 and 3.

Synthesis

Unless noted otherwise, all reagents and solvents were purchased from commercial sources and used as received. All reactions were performed in a screw-capped vial. The proton (^{1}H) and carbon (^{13}C) NMR spectra were obtained using a 500 MHz using Me_4Si as an internal standard and are reported in δ units. Coupling constants (*J* values) are reported in Hz. Column chromatography was performed on silica gel using flash chromatography (Teledyne ISCO EZprep). High-resolution mass spectra (HRMS) were obtained using the electron spray ionization (ESI) technique and as TOF mass analyzer. Organic solvents and starting materials were used as received. The BMS compound **4a** (BMS-1 or KPGC01S94)[7] as well as compounds **4b-c** were synthesized according to the reported procedures starting from compound **1, 2a-b, 3a-b** and spectral data were in accordance with reported data. [6–8]

Compound 4a (BMS-1 or KPGC01S94), (*S*)-1-(2,6-dimethoxy-4-((2-methyl-[1,1'-biphenyl]-3-yl)methoxy)benzyl)piperidine-2-carboxylic acid: **3b** from scheme 1 (45 mg, 0.125 mmol), (S)-piperidine-2-carboxylic acid (64.5 mg, 4 equiv, 0.5 mmol), sodium cyanoborohydride (40.8 mg, 5.2 equiv, 0.65 mmol), were dissolved in DMF (1 mL) and then added acetic acid (2 drops). The reaction mixture was allowed to stir at 80 ^{o}C for 1 hour. The reaction was monitored by TLC. The crude was purified by 0-20% MeOH:DCM to afford desire product as an off-white solid (31.5 mg, 53% yield). ^{1}H NMR (500 MHz, DMSO-*d*$_6$) *δ* 7.49 – 7.41 (m, 3H), 7.39 – 7.34 (m, 1H), 7.32 – 7.25 (m, 3H), 7.19 (dd, *J* = 7.7, 1.5 Hz, 1H), 6.41 (s, 2H), 5.17 (s, 2H), 4.08 (s, 2H), 3.78 (s, 7H), 3.11 (t, *J* = 5.5, 5.5 Hz, 1H), 3.08 – 2.99 (m, 1H), 2.60 (dd, *J* = 13.5, 6.7 Hz, 1H), 2.20 (s, 3H), 1.80 (q, *J* = 6.0, 5.9, 5.9 Hz, 2H), 1.55 (q, *J* = 6.7, 6.1, 6.1 Hz, 2H), 1.37 (ddt, *J* = 18.4, 12.8, 6.5, 6.5 Hz, 3H); ^{13}C NMR (126 MHz, DMSO-*d*$_6$) *δ* 172.0, 161.47, 160.32, 142.70, 141.85, 135.83, 134.59, 130.25, 129.63, 128.86, 128.72, 127.44, 126.04, 92.05, 69.23, 64.35, 56.42, 48.70, 46.21, 31.16, 26.11, 22.13, 21.27, 16.41.

Compound 4b (KPGC01S32), (4-((3-(2,3-dihydrobenzo[*b*][1,4]dioxin-6-yl)-2-methylbenzyl)oxy)-2,6-dimethoxybenzyl)-D-serine: **3a** from scheme 1 (35.6 mg, 0.104 mmol), D-serine (32.8 mg, 3 equiv), sodium cyanoborohydride (19.6 mg, 3 equiv), were dissolved in DMF (1 mL) and then added acetic acid (0.104 mmol, 1 equiv, 2 drops). The reaction mixture was allowed to stir overnight at room temperature. The reaction was monitored by TLC. The crude was purified by 0-20% MeOH:DCM to afford desire product as an off-white solid (42% yield). ^{1}H NMR (500 MHz, DMSO-*d*$_6$) *δ* 7.42 (dd, J = 7.6, 1.5 Hz, 1H), 7.22 (t, J = 7.6, 7.6 Hz, 1H), 7.15 (dd, J = 7.6, 1.5 Hz, 1H), 6.90 (d, J = 8.2 Hz, 1H), 6.76 (d, J = 2.1 Hz, 1H), 6.73 (dd, J = 8.2, 2.1 Hz, 1H), 6.37 (s, 2H), 5.13 (s, 2H), 4.26 (s, 4H), 3.86 (s, 2H), 3.77 (s, 6H), 3.58 (dt, J = 8.5, 3.4, 3.4 Hz, 2H), 2.94 (t, J = 6.0, 6.0 Hz, 1H, NH), 2.20 (s, 3H); ^{13}C NMR (126 MHz, DMSO-d_6) δ 172.85, 160.75, 159.69, 159.53, 143.42, 142.96, 142.12, 135.85, 134.96, 134.65, 130.20, 128.56, 125.93, 122.59, 118.17, 117.26, 104.65, 92.06, 69.18, 64.57, 62.51, 61.34, 56.43, 56.32, 16.41; HRMS (ESI): for $C_{28}H_{32}NO_8$ [M + H]$^+$ found, 510.2132 m/z; calculated mass, 510.2128.

Compound 4c (KPGC01S138), *N*-(2,6-dimethoxy-4-((2-methyl-[1,1'-biphenyl]-3-yl)methoxy) benzyl)-3,3,3-trifluoro-1-phenylpropan-1-amine: 3b from scheme 1 (8 mg, 0.022 mmol), 3,3,3-trifluoro-1-phenylpropan-1-amine (16.7 mg, 0.088 mmol, 4 equiv), sodium cyanoborohydride (7.2 mg, 0.114 mmol, 5.2 equiv), were dissolved in DMF (0.5 mL) and then added acetic acid (1 drop). The reaction mixture was allowed to stir at 80 °C for 3 hours. The reaction was monitored by TLC. The crude was purified by 0-20% MeOH:DCM to afford desire product as oily product (68% yield). ^{1}H NMR (500 MHz, CDCl$_3$) δ 7.45 – 7.38 (m, 5H), 7.38 – 7.30 (m, 6H), 7.30 – 7.27 (m, 1H), 7.26 (d, *J* = 5.4 Hz, 1H), 6.22 (s, 2H), 5.08 (s, 2H), 3.96 (t, *J* = 6.5, 6.5 Hz, 1H), 3.75 (s, 6H), 3.73 (d, *J* = 6.5 Hz, 2H), 2.46 (s, 1H), 2.27 (s, 3H), 1.29 – 1.24 (m, 1H); ^{13}C NMR (126 MHz, CDCl$_3$) δ 160.23, 159.41, 143.06, 141.94, 135.1, 134.49, 132.81, 130.34, 129.40, 128.49, 128.32, 128.11, 127.91, 127.62, 127.18, 126.90, 125.65, 91.17, 69.34, 56.21, 55.53, 39.11, 16.23; HRMS (ESI): for $C_{32}H_{33}F_3NO_3$[M + H]$^+$ found, 536.2419 m/z; calcd mass, 536.2413.

Compound 4d (GCL.2), (*7R,8R,9S,13S,14S,17R*)-17-ethynyl-17-hydroxy-7,13-dimethyl-1,2,6,7,8,9,10,11,12,13,14,15,16,17-tetradecahydro-3*H*-cyclopenta[a]phenanthren-3-one: Tibolone (156 mg, 0.5 mmol) was taken in a round bottom flask containing 10 mL of THF and 100 µL of water was added. Next, *p*-toluene sulfonic acid (85 mg, 0.5 mmol) was added to it and the mixture was refluxed at 80 °C for 48 hours and the progress of the reaction was monitored by TLC. The organic solvent was then evaporated to dryness to get the crude product, which was purified by flash column chromatography using 20% ethyl acetate in pet-ether solvent mixture as eluent to give off-white solid pure compound GCL2 (53% yield). ^{1}H NMR (500 MHz, MeOD) δ 5.80 (t, J = 2.1, 2.1 Hz, 1H), 2.88 (s, 1H), 2.56 (ddt, J = 14.1, 5.4, 1.6, 1.6 Hz, 1H), 2.42 – 2.28 (m, 4H), 2.27 – 2.19 (m, 1H), 2.18 – 2.13 (m, 1H), 2.06 – 1.90 (m, 3H), 1.77 – 1.53 (m, 6H), 1.44 – 1.25 (m, 2H), 1.14 (qd, J = 11.0, 11.0, 10.9, 4.2 Hz, 1H), 0.91 (d, J = 0.7 Hz, 3H), 0.79 (d, J = 7.1 Hz, 3H). ^{13}C NMR (126 MHz, MeOD) δ 201.06, 167.84, 125.32, 87.28, 78.82, 73.45, 48.12, 47.95, 47.78, 47.61, 47.44, 47.27, 47.10, 46.67, 45.82, 43.05, 42.76, 42.18, 38.28, 36.02, 32.25, 30.66, 26.44, 26.41, 21.71, 11.79, 11.77.

ASSOCIATED CONTENT

Supporting Information

The Supporting Information is available free of charge on the ACS Publications website at DOI: xxx-xxx-xxx.

AUTHOR INFORMATION

Corresponding Author

*E-mail: gchopra@purdue.edu

ORCID

Gaurav Chopra: 0000-0003-0942-7898

Author Contributions

# P.R.W., J.A.F. and K.P.J. contributed equally to this work. P.R.W. and K.P.J. synthesized and characterized all the compounds. P.R.W. performed all docking calculations. P.R.W. and J.A.F. implemented the EGNN machine learning model and analyzed model performance. P.R.W. performed all IC_{50} experiments and analyzed the data. G.C. conceived the idea and supervised the study. All authors discussed the models, experiments, wrote, and edited the manuscript and have given approval to the final version of the manuscript.

Notes

The authors declare no competing financial interest.

ACKNOWLEDGMENTS

This research was supported by Startup Funds from Department of Chemistry at Purdue University and Integrative Data Science Initiative award to G.C. Additional support, in part, by a NCATS Clinical and Translational Sciences Award from the Indiana Clinical and Translational Sciences Institute (UL1TR002529). The authors acknowledge the support from the Purdue University Center for Cancer Research, NIH grant P30 CA023168. The content is solely the responsibility of the authors and does not necessarily represent the official views of the National Institutes of Health.

ABBREVIATIONS USED

PD-1 programmed cell death-1; PD-L1 programmed death-ligand-1; GNN graph neural network; EGNN energy graph neural network; SVM support vector machines; RF random forest; FDA, U.S. Food and Drug Administration; HTRF, homogeneous time-resolved fluorescence; PPh_3, triphenylphosphine; DIAD, Diisopropyl azodicarboxylate; THF, tetrahydrofuran; Me_4Si Tetramethylsilane; ML, machine learning; AUROC, Area Under the Receiver Operator Characteristic.

REFERENCES

(1) Pardoll, D. M. The Blockade of Immune Checkpoints in Cancer Immunotherapy. *Nat. Rev. Cancer* **2012**, *12* (4), 252–264.

(2) Buchbinder, E. I.; Desai, A. CTLA-4 and PD-1 Pathways Similarities, Differences, and Implications of Their Inhibition. *American Journal of Clinical Oncology: Cancer Clinical Trials*. Wolters Kluwer Health 2016, pp 98–106.

(3) Sasikumar, P. G. N.; Ramachandra, M.; Naremaddepalli, S. S. S. 1, 2, 4-Oxadiazole Derivatives as Immunomodulators. Google Patents September 2017.

(4) Sunshine, J.; Taube, J. M. Pd-1/Pd-L1 Inhibitors. *Curr. Opin. Pharmacol.* **2015**, *23*, 32–38.

(5) Imai, K.; Takaoka, A. Comparing Antibody and Small-Molecule Therapies for Cancer. *Nat. Rev. Cancer* **2006**, *6* (9), 714–727.

(6) Chupak, L.; Ding, M.; Martin, S.; Zheng, X.; Hewawasam, P.; Connoly, T.; Xu, N.; Yeung, K.; Zhu, J.; Langley, D.; et al. Compounds Useful as Immunomodulators. WO/2015/160641, October 22, 2015.

(7) Chupak, L. S.; Zheng, X.; Mingo, P. A. Compounds Useful as Immunomodulators. WO/2015/034820, December 3, 2015.

(8) Guzik, K.; Zak, K. M.; Grudnik, P.; Magiera, K.; Musielak, B.; Törner, R.; Skalniak, L.; Dömling, A.; Dubin, G.; Holak, T. A. Small-Molecule Inhibitors of the Programmed Cell Death-1/Programmed Death-Ligand 1 (PD-1/PD-L1) Interaction via Transiently Induced Protein States and Dimerization of PD-L1. *J. Med. Chem.* **2017**, *60* (13), 5857–5867.

(9) Zak, K. M.; Grudnik, P.; Guzik, K.; Zieba, B. J.; Musielak, B.; Dömling, A.; Dubin, G.; Holak, T. A. Structural Basis for Small Molecule Targeting of the Programmed Death Ligand 1 (PD-L1). *Oncotarget* **2016**, *7* (21), 30323–30335.

(10) Broach, J. R.; Thorner, J. High-Throughput Screening for Drug Discovery. *Nature*. [London: Macmillan Journals], 1869- 1996, pp 14–16.

(11) Artis, D. R.; Lin, J. J.; Zhang, C.; Wang, W.; Mehra, U.; Perreault, M.; Erbe, D.; Krupka, H. I.; England, B. P.; Arnold, J.; et al. Scaffold-Based Discovery of Indeglitazar, a PPAR Pan-Active Anti-Diabetic Agent. *Proc. Natl. Acad. Sci. U. S. A.* **2009**, *106* (1), 262–267.

(12) Böhm, H.-J.; Flohr, A.; Stahl, M. Scaffold Hopping. *Drug Discov. today Technol.* **2004**, *1* (3), 217–224.

(13) Kitchen, D. B.; Decornez, H.; Furr, J. R.; Bajorath, J. Docking and Scoring in Virtual Screening for Drug Discovery: Methods and Applications. *Nat. Rev. Drug Discov.* **2004**, *3* (11), 935–949.

(14) Joachims, T. Text Categorization with Support Vector Machines: Learning with Many Relevant Features. *Lect. Notes Comput. Sci. (including Subser. Lect. Notes Artif. Intell. Lect. Notes Bioinformatics)* **1998**, *1398*, 137–142.

(15) Burbidge, R.; Trotter, M.; Buxton, B.; Holden, S. Drug Design by Machine Learning: Support Vector Machines for Pharmaceutical Data Analysis. *Comput. Chem.* **2001**, *26* (1), 5–14.

(16) Heikamp, K.; Bajorath, J. Support Vector Machines for Drug Discovery. *Expert Opin. Drug*

Discov. **2014**.

(17) Breiman, L. Random Forests. *Mach. Learn.* **2001**, *9* (1), 5–32.

(18) Li, H.; Leung, K. S.; Wong, M. H.; Ballester, P. J. Improving Autodock Vina Using Random Forest: The Growing Accuracy of Binding Affinity Prediction by the Effective Exploitation of Larger Data Sets. *Mol. Inform.* **2015**, *34* (2–3), 115–126.

(19) Zhang, Q. Y.; Aires-de-Sousa, J. Random Forest Prediction of Mutagenicity from Empirical Physicochemical Descriptors. *J. Chem. Inf. Model.* **2007**, *47* (1), 1–8.

(20) Torng, W.; Altman, R. B. Graph Convolutional Neural Networks for Predicting Drug-Target Interactions. *J. Chem. Inf. Model.* **2019**.

(21) Scarselli, F.; Gori, M.; Tsoi, A. C.; Hagenbuchner, M.; Monfardini, G. The Graph Neural Network Model. *IEEE Trans. Neural Networks* **2009**, *20* (1), 61–80.

(22) Lim, J.; Ryu, S.; Park, K.; Choe, Y. J.; Ham, J.; Kim, W. Y. Predicting Drug–Target Interaction Using a Novel Graph Neural Network with 3D Structure-Embedded Graph Representation. *J. Chem. Inf. Model.* **2019**, *59* (9), 3981–3988.

(23) Ma, T.; Zhang, A. *AffinityNet: Semi-Supervised Few-Shot Learning for Disease Type Prediction*.

(24) Tsubaki, M.; Tomii, K.; Sese, J. Compound-Protein Interaction Prediction with End-to-End Learning of Neural Networks for Graphs and Sequences. *Bioinformatics* **2019**, *35* (2), 309–318.

(25) Gupta, A.; Müller, A. T.; Huisman, B. J. H.; Fuchs, J. A.; Schneider, P.; Schneider, G.

Generative Recurrent Networks for De Novo Drug Design. *Mol. Inform.* **2018**, *37* (1).

(26) Ståhl, N.; Falkman, G.; Karlsson, A.; Mathiason, G.; Boström, J. Deep Reinforcement Learning for Multiparameter Optimization in de Novo Drug Design. *J. Chem. Inf. Model.* **2019**.

(27) Li, Y.; Zhang, L.; Liu, Z. Multi-Objective de Novo Drug Design with Conditional Graph Generative Model. *J. Cheminform.* **2018**, *10* (1).

(28) Esaki, T.; Ohashi, R.; Watanabe, R.; Natsume-Kitatani, Y.; Kawashima, H.; Nagao, C.; Mizuguchi, K. Computational Model to Predict the Fraction of Unbound Drug in the Brain. *J. Chem. Inf. Model.* **2019**.

(29) Fine, J.; Chopra, G. Lemon: A Framework for Rapidly Mining Structural Information from the Protein Data Bank. *Bioinformatics* **2019**.

(30) Chopra, G.; Samudrala, R. Exploring Polypharmacology in Drug Discovery and Repurposing Using the CANDO Platform. *Curr. Pharm. Des.* **2016**, *22* (21), 3109–3123.

(31) Fine, J.; Konc, J.; Samudrala, R.; Chopra, G. CANDOCK: Chemical Atomic Network Based Hierarchical Flexible Docking Algorithm Using Generalized Statistical Potentials. *bioRxiv* **2018**.

(32) Kischuk, E.; Majumder, J.; Fine, J. A.; Lantz, T. C.; Dhawan, D.; Knapp, D. W.; Ratliff, T. L.; Chopra, G. Abstract 4709: Cell-Specific Gene Program-Based Small-Molecule Immunomodulators Targeting Solid-Tumor Microenvironments; 2018.

(33) Esensten, J. H.; Helou, Y. A.; Chopra, G.; Weiss, A.; Bluestone, J. A. CD28 Costimulation:

From Mechanism to Therapy. *Immunity*. 2016, pp 973–988.

(34) Hernandez-Perez, M.; Chopra, G.; Fine, J.; Conteh, A. M.; Anderson, R. M.; Linnemann, A. K.; Benjamin, C.; Nelson, J. B.; Benninger, K. S.; Nadler, J. L.; et al. Inhibition of 12/15-Lipoxygenase Protects Against β-Cell Oxidative Stress and Glycemic Deterioration in Mouse Models of Type 1 Diabetes. *Diabetes* **2017**, *66* (11), 2875–2887.

(35) Ma, X.; Zhou, J.; Wang, C.; Carter-Cooper, B.; Yang, F.; Larocque, E.; Fine, J.; Tsuji, G.; Chopra, G.; Lapidus, R. G.; et al. Identification of New FLT3 Inhibitors That Potently Inhibit AML Cell Lines via an Azo Click-It/Staple-It Approach. *ACS Med. Chem. Lett.* **2017**, *8* (5).

(36) Fine, J.; Lackner, R.; Samudrala, R.; Chopra, G. Computational Chemoproteomics to Understand the Role of Selected Psychoactives in Treating Mental Health Indications. *Sci. Rep.* **2019**.

(37) Lu, L.; Zhang, F.; Li, J.; Wang, H.; Xiao, K.; Wu, L.; Qian, D.-Q.; Lajkiewicz, N.; Konkol, L.; Li, Z.; et al. Heterocyclic Compounds Derivatives as PD-L1 Internalization Inducers. WO/2018/119263, June 28, 2018.

(38) Xiao, K.; Zhang, F.; Wu, L.; Yao, W. Heterocyclic Compounds as Immunomodulators. US 2018/0273519 A1, September 27, 2018.

(39) Willett, P. Similarity-Based Virtual Screening Using 2D Fingerprints. *Drug Discov. Today* **2006**, *11* (23–24), 1046–1053.

(40) DeLano, W. L. *Pymol: An Open-Source Molecular Graphics Tool*; CCP4, 2002; Vol. 40.

(41) Max, K.; Weston, S.; Keefer, C.; Engelhardt, A.; Cooper, T.; Mayer, Z.; Kenkel, B.; Team, R.

C.; Benesty, M.; Lescarbeau, R.; et al. Classification and Regression Training. 2016, p 198.

(42) Robin, X.; Turck, N.; Hainard, A.; Tiberti, N.; Lisacek, F.; Sanchez, J. C.; Müller, M. PROC: An Open-Source Package for R and S+ to Analyze and Compare ROC Curves. *BMC Bioinformatics* **2011**, *12* (1), 77.

(43) Guzik, K.; Tomala, M.; Muszak, D.; Konieczny, M.; Hec, A.; Błaszkiewicz, U.; Pustuła, M.; Butera, R.; Dömling, A.; Holak, T. A. Development of the Inhibitors That Target the PD-1/PD-L1 Interaction—A Brief Look at Progress on Small Molecules, Peptides and Macrocycles. *Molecules* **2019**, *24* (11), 2071.

(44) Zak, K. M.; Kitel, R.; Przetocka, S.; Golik, P.; Guzik, K.; Musielak, B.; Dömling, A.; Dubin, G.; Holak, T. A. Structure of the Complex of Human Programmed Death 1, PD-1, and Its Ligand PD-L1. *Structure* **2015**.

(45) Lee, H. T.; Lee, S. H.; Heo, Y. S. Molecular Interactions of Antibody Drugs Targeting PD-1, PD-L1, and CTLA-4 in Immuno-Oncology. *Molecules*. 2019.

(46) Zak, K. M.; Grudnik, P.; Magiera, K.; Dömling, A.; Dubin, G.; Holak, T. A. Structural Biology of the Immune Checkpoint Receptor PD-1 and Its Ligands PD-L1/PD-L2. *Structure*. 2017.

(47) PyTorch Community. Tensors and Dynamic Neural Networks in Python with Strong GPU Acceleration. *Github* **2016**, *6*.

(48) Chemaxon, M. Molecule File Converter, Version 5.10. 1,(C) 1999− 2012 ChemAxon Ltd.

(49) Landrum, G. A. RDKit: Open-Source Cheminformatics.

(50) Costa, F.; De Grave, K. Fast Neighborhood Subgraph Pairwise Distance Kernel. In *ICML*

2010 - Proceedings, 27th International Conference on Machine Learning; Omnipress; Madison, WI, USA, 2010; pp 255–262.

(51) Csizmadia, P. MarvinSketch and MarvinView: Molecule Applets for the World Wide Web. In *Proceedings of ECSOC-3, the third international electronic conference on synthetic organic chemistry, September 1ą30*; 2019; p 1775.

Table of Contents graphic